Journal of the Mechanics and Physics of Solids 59 (2011) 713–731

Contents lists available at ScienceDirect

Journal of the Mechanics and Physics of Solids

journal homepage: www.elsevier.com/locate/jmps

Nonlocal continuum crystal plasticity with internal residual stresses

Ramin Aghababaei [a], Shailendra P. Joshi [a,*], J.N. Reddy [b]

[a] Department of Mechanical Engineering, National University of Singapore, Singapore
[b] Department of Mechanical Engineering, Texas A&M University, College Station, TX, USA

ARTICLE INFO

Article history:
Received 5 August 2010
Accepted 6 November 2010
Available online 18 November 2010

Keywords:
Strengthening and mechanisms
Slip gradients
Crystal plasticity
Residual stress

ABSTRACT

We derive a three-dimensional constitutive theory accounting for length-scale dependent internal residual stresses in crystalline materials that develop due to a non-homogeneous spatial distribution of the excess dislocation (edge and screw) density. The second-order internal stress tensor is derived using the Beltrami stress function tensor $\boldsymbol{\varphi}$ that is related to the Nye dislocation density tensor. The formulation is derived explicitly in a three-dimensional continuum setting for elastically isotropic materials. The internal stresses appear as additional resolved shear stresses in the crystallographic visco-plastic constitutive law for individual slip systems. Using this formulation, we investigate two boundary value problems involving single crystals under symmetric double slip. In the first problem, the response of a geometrically imperfect specimen subjected to monotonic and cyclic loading is investigated. The internal stresses affect the overall strengthening and hardening under monotonic loading, which is mediated by the severity of initial imperfections. Such imperfections are common in miniaturized specimens in the form of tapered surfaces, fillets, fabrication induced damage, etc., which may produce strong gradients in an otherwise nominally homogeneous loading condition. Under cyclic loading the asymmetry in the tensile and compressive strengths due to this internal stress is also strongly influenced by the degree of imperfection. In the second example, we consider simple shear of a single crystalline lamella from a layered specimen. The lamella exhibits strengthening with decreasing thickness and increasing lattice incompatibility with shearing direction. However, as the thickness to internal length-scale ratio becomes small the strengthening saturates due to the saturation of the internal stress.

Finally, we present the extension of this approach for crystalline materials exhibiting elastic anisotropy, which essentially depends on the appropriate Green function within $\boldsymbol{\varphi}$.

1. Introduction

Conventional continuum plasticity theories are size-independent and treat the plastic behavior of crystalline metals as a material response that does not depend on geometric or microstructural length-scales. However, there are compelling experimental evidences of strong strengthening in nanostructured materials compared to their coarse-grained counterparts. Experiments on miniaturized specimens also suggest that the yield strength ceases to be a purely material parameter as the specimen dimensions approach characteristic microstructural length-scales such as grain size, cell-wall spacing, dislocation spacing, etc. At these length-scales, the mechanisms of plasticity may be significantly altered giving rise to macroscopic phenomena such as strong strengthening and modified hardening that are intimately tied to the microstructural and macrostructural details. To explain some of the experimentally observed length-scale effects, traditional continuum mechanics of plastic deformation is augmented with a variety of

* Corresponding author. Tel.: +65 6516 4496; fax: +65 6779 1459.
E-mail addresses: ramin.aghababaei@nus.edu.sg (R. Aghababaei), Shailendra@nus.edu.sg (S.P. Joshi).

0022-5096/$ - see front matter © 2010 Elsevier Ltd. All rights reserved.
doi:10.1016/j.jmps.2010.11.003

mechanisms such as strain gradients (Fleck and Hutchinson, 1993), dislocation starvation, limited dislocation sources (Dehm, 2009; Uchic et al., 2009), etc. In practice, such effects may operate in tandem and may contribute synergistically or compete with each other to produce overall plastic responses. Of the different mechanism-based length-scale dependent plasticity theories, nonlocal approaches incorporating strain gradients have gained popularity. Such approaches invoke the existence of excess dislocations[1] that are necessary to maintain geometric compatibility during plastic deformation. There are several versions of the gradient plasticity theories available in literature, but the core concept is the assumption that the local kinematics and kinetics of deformation at a continuum point is modulated by its surrounding points. The introduction of a gradient term introduces a length-scale in to the conventional plasticity and endows it with an ability to predict length-scale dependent plastic behavior. In this work, we formulate a nonlocal approach based on continuum dislocation theory that augments the classical crystal plasticity theory with length-scale dependent internal residual stresses. First, we briefly summarize some of the strain gradient plasticity theories with reference to their salient features incorporating first and higher gradients of strain.

Fleck and Hutchinson (1993) introduced higher-order stresses corresponding to the first gradient of plastic strain in the classical plasticity theory to model the length-scale dependent responses in micro-beam bending, torsion of micro-wires and micro-indentation. Gao and co-workers (Gao et al., 1999; Nix and Gao, 1998) provided a physical basis for the microstructural length-scale in their Mechanism-Based Strain Gradient (MSG) plasticity theory that was based on the Taylor hardening model. Han et al. (2005a, 2005b) extended the MSG theory to crystal plasticity. These theories requiring higher-order boundary conditions have been further refined to include thermodynamically consistent descriptions of the dislocation density (e.g. Abu Al-Rub et al., 2007). On the other hand, lower order theories (Acharya and Bassani, 2000; Huang et al., 2004; Shu et al., 2001) avoid the complicating features of the higher-order theories by neglecting the higher-order stresses in the governing equations. Recently, Evans and Hutchinson (2009) compared the lower-order and higher-order gradient theories and showed that even in the case of first-gradient theories the nature of the length-scale dependent formulation may exhibit either strengthening at yield or an enhancement in hardening after yield.

Another class of gradient theories includes second gradients of strains in a mathematical sense (Bazant and Pijaudier-Cabot, 1988; Eringen, 1983) or from a phenomenological viewpoint (e.g. Aifantis, 1984, 1999). Recent approaches based on second gradients of plastic strains formulate the length-scale dependent plasticity in a thermodynamically consistent manner (Bardella, 2006, 2007; Gurtin, 2000, 2002; Gurtin and Anand, 2007) ascribing their presence to the distribution of defects. These approaches predict enhanced strengthening, hardening and the internal stress (aka back-stress) induced asymmetry in the tension-compression cyclic response (the Bauschinger effect) as a function of microstructural parameters. Acharya and Roy (2006) developed a phenomenological mesoscopic field dislocation mechanics approach (PMFDM) that accounts for GNDs in the dissipative and energetic sense based on incompatible elastic distortions. Ertürk et al. (2009), Evers et al. (2004); Gerken and Dawson (2008) and Kuroda and Tvergaard (2008a, b) developed physically based, crystal plasticity theories in that the back-stress that determines the effective (i.e. applied stress plus the size-dependent back-stress) shear stress for plastic slip on a slip plane is derived using the Volterra dislocation theory. Concurrently, Yefimov et al. (2004) derived similar expressions for the effective shear stress on a slip plane corresponding to the edge dislocation density using statistical-mechanics approach. These different approaches provide a similar computational construct and may be interpreted in terms of each other Kuroda and Tvergaard (2006).

In this paper, we formulate a stress function based approach to derive length-scale dependent three-dimensional (3D) internal residual stress tensor due to the non-homogeneous spatial distribution of the GND density using continuum dislocation theory. Invoking the Beltrami stress function tensor $\boldsymbol{\varphi}$ (Sadd, 2005), we systematically relate the length-scale dependent internal residual stress tensor $\mathbf{T}^*$ to the gradient of the Nye dislocation density tensor $\mathbf{A}$ via the constitutive equations for a bulk, linear elastic solid.[2] This 3D internal stress tensor that automatically includes the effects of both, edge and screw GNDs is described in terms of the incompatible parts of the continuum kinematic variables, namely the elastic strain and curvature tensors. The definition of $\mathbf{T}^*$ via $\boldsymbol{\varphi}$ ensures its equilibrium and can naturally blend into the conventional equilibrium equation. The higher order derivatives of the Green function in $\mathbf{T}^*$ decay rapidly with distance introducing a length-scale that has to be related to the microstructural details of a boundary value problem (bvp). This length-scale dependent continuum framework is then extended to the crystal plasticity theory using the kinematics and kinetics of crystallographic slip, expressed in a thermodynamically consistent manner (Gurtin, 2002; Kuroda and Tvergaard, 2008b).

We consider two bvps involving single crystals under plane strain condition with symmetric double slip, namely, (i) a tapered specimen under uniaxial loading (ignoring the free surface effects), and (ii) constrained simple shear of a single lamella with impenetrable boundaries, from a layered microstructure that mimics a nano-twinned grain. The importance of the size-dependent hardening mechanisms is highlighted through these examples. The results are discussed within the context of the experimental/computational investigations reported in the literature on the length-scale dependent single crystal plasticity under monotonic and cyclic loading.

2. Background

As an illustration to distinguish between the length-scale dependent hardening mechanisms due to the GND density, we consider two examples of crystalline lattices subjected to curvatures. Here, we do not account for the free surfaces by

[1] These are commonly referred to as the Geometrically Necessary Dislocations (GNDs) (Nye, 1953).
[2] A short discussion for elastically anisotropic solids is presented in Appendix B.

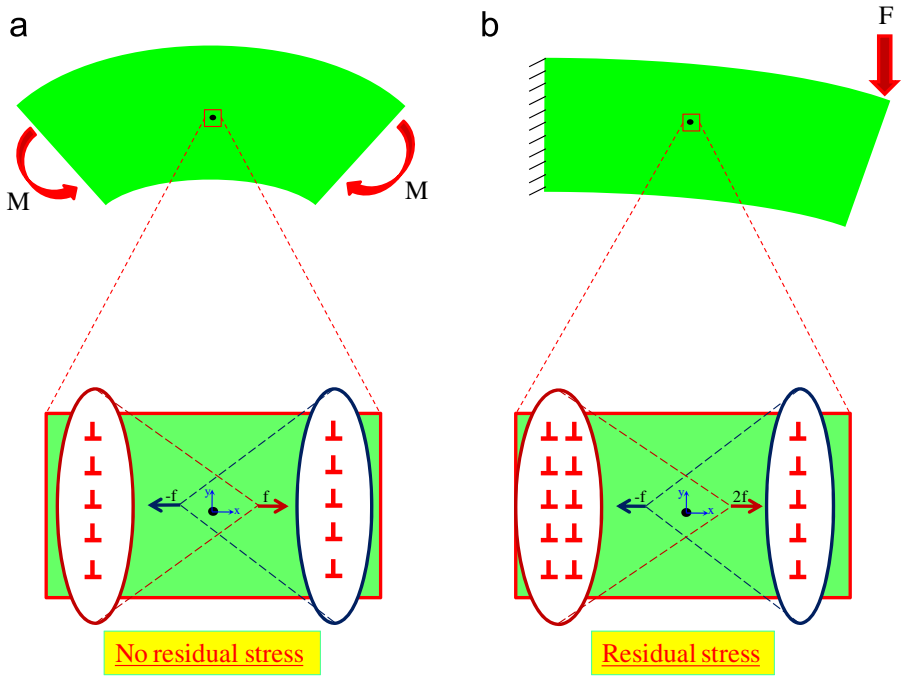

Fig. 1. Examples illustrating the contributions of GND density to enhanced hardening in (a) pure beam bending—dissipative hardening, (b) non-uniform bending—dissipative and energetic hardening.

implicitly assuming that the crystal lattice is embedded in an elastic region of same elastic properties (Mesarovic et al., 2010). Fig. 1a shows the surrounding region of a continuum point wherein the crystal lattice is under pure bending resulting in constant lattice curvature (Fleck and Hutchinson, 1993). In this region, the non-uniform strain along the x_2 axis results in a non-zero GND density component A_{31} that is proportional to the curvature κ_{13} (Nye, 1953). However, at any section along the x_1 direction the curvature is a constant ($=\kappa$) and therefore, the GND density component is also homogeneously distributed along the x_1 axes. Consequently, at any continuum point the average stress fields due to the presence of the GNDs cancel out. In this problem, the size-dependent hardening mechanism is related to the presence of GND density which is the dissipative hardening mechanism and corresponds to the first gradient of plastic strain (e.g. Nix and Gao, 1998; Acharya and Bassani, 2000). However, in the second case (Fig. 1b) the lattice curvature varies linearly along the x_1 direction and correspondingly, the GND density also varies linearly (i.e. $A_{31}=ax_1+b$, where a and b are constants characterized by the applied stimulus and material compliance). As demonstrated later, this leads to two contributions to hardening, one purely due to the presence of the GND density similar to the first illustration and an additional term due to a net internal stress that exists owing to its non-homogeneous distribution, as their average stress fields at a continuum point may not cancel out. The resulting hardening is sometimes referred to as energetic hardening. Therefore, this internal residual stress because of the non-zero gradient of the GND density together with the dissipative hardening mechanism must be accounted for to predict both the size-dependent hardening mechanisms.

In discrete dislocation plasticity the internal stress enters the formulation through the Peach–Koehler force acting on a dislocation[3] (e.g. Van der Giessen and Needleman, 1995)

$$\mathbf{p}^i=-\mathbf{l}^i\times\left(\mathbf{T}^{ext}+\sum_{j\neq i}\mathbf{T}^*_j\right)\times\mathbf{b}^i \tag{1}$$

where $\mathbf{p}^i$ is the Peach–Koehler force vector on ith dislocation, $\mathbf{b}^i$ is the Burgers vector for that dislocation, $\mathbf{l}^i$ is its unit tangent vector and $\mathbf{T}^{ext}$ is the applied stress. $\mathbf{T}^*_j$ is the internal stress field from the jth on the ith dislocation, which is superposed over all dislocations. While these length-scale dependent internal stresses may not play a big role in the response of conventional bulk crystalline materials, experiments show that it cannot be ignored in the regimes where the microstructural length-scales mediate the macroscopic response. For example, thin-film tension and cyclic bending experiments by Xiang and Vlassak (2006) exhibit length-scale mechanics of strengthening and the Bauschinger effect in passivated specimens compared with the unpassivated ones. In this case, the passivation layers act as hard boundaries that obstruct dislocations escaping through the

[3] *Notations*: In this paper, we use italic-no boldface for scalars (*a, b,*…); lower-case boldface for vectors (**a, b**,…); upper-case boldface for second- and higher-order tensors (**A, B,** …).
$\nabla(\cdot)$, $div(\cdot)$, $curl(\cdot)$ and $inc(\cdot)$ represent the gradient, divergence, curl and $\varepsilon_{kni}\varepsilon_{lmj}(\cdot)_{kl,nm}$, respectively, where ε_{kni} is the permutation symbol.
$(\cdot)_{,i}$ indicates the partial derivative of a quantity with respect to x_i and $\mathbf{a}\otimes\mathbf{b}$ indicates a tensor product to two vectors.

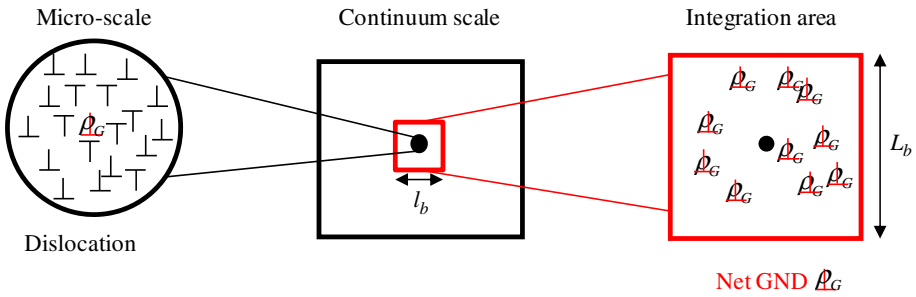

Fig. 2. Schematic illustrating the non-locality arising from the presence of GND density at a continuum point and the distribution of the GND density around that point.

surfaces, leading to the accumulation of dislocations necessary to accommodate geometric incompatibilities. Very recently, Kiener et al. (2010) experimentally observed the Bauschinger effect in single crystal Cu micro-beams under cantilever bending. Even under nominally homogeneous loading conditions such as uniaxial compression or tension the strain and curvature gradients may be induced in miniaturized specimens by virtue of geometric imperfections or fabrication defects that may play vital roles in the strengthening and hardening of single crystal specimens (El-Awady et al., 2009a, 2009b; Frick et al., 2008).

Unlike the discrete dislocation modeling where the superposition of the stress fields due to individual dislocations produces an inherently nonlocal theory (Van der Giessen and Needleman, 1995), in homogenized approaches that smear out the discreteness of dislocations we must adopt a length-scales dependent approach to account for the internal stresses due to dislocation arrangement (Fig. 2).

3. Kinematics of compatible and incompatible deformation

In continuum mechanics, the deformation gradient tensor ($\mathbf{F}$) is

$$\mathbf{F}=\mathbf{I}+\mathbf{B} \tag{2}$$

where $\mathbf{B}=\nabla\mathbf{u}$ is the total displacement gradient tensor. Under small deformation and small strain assumptions, the total displacement gradient tensor $\mathbf{B}$ may be additively decomposed into the elastic and plastic parts[4]

$$\mathbf{B}=\mathbf{B}^e+\mathbf{B}^p \tag{3}$$

Further,

$$\mathbf{B}=\underbrace{\tfrac{1}{2}(\mathbf{B}+\mathbf{B}^T)}_{\mathbf{E}}+\underbrace{\tfrac{1}{2}(\mathbf{B}-\mathbf{B}^T)}_{\mathbf{W}} \tag{4}$$

where $\mathbf{E}$ is the infinitesimal strain tensor and $\mathbf{W}$ is the infinitesimal rotation tensor. Further, we assume additive decomposition of the elastic and plastic strains into their compatible and incompatible parts[5]

$$\mathbf{E}^e=\mathbf{E}^e_C+\mathbf{E}^e_I \tag{5}$$

and[6]

$$\mathbf{E}^p=\mathbf{E}^p_C+\mathbf{E}^\mathbf{p}_I \tag{6}$$

The incompatible part of the elastic strain tensor $\mathbf{E}^e_I$ may be obtained from the strain compatibility conditions. In the presence of internal defects such as dislocations the requirement of compatibility of the total strain introduces an incompatibility tensor $\mathbf{N}$ (Kröner, 1959)

$$N_{kl}=\varepsilon_{ijk}\varepsilon_{lmn}(E^e_I)_{in,jm}=-\varepsilon_{ijk}\varepsilon_{lmn}(E^p_I)_{in,jm} \tag{7}$$

In Eq. (7) the incompatibility tensor, obtained as the second gradient of the elastic (or plastic) strain tensor, is a measure of the deviation of the elastic (or the plastic) strains from their compatible counterparts due to the presence of excess dislocations that result in internal stresses in addition to those due to the applied loads. For convenience, we set $\varepsilon_{kni}\varepsilon_{lmj}(\cdot)_{kl,nm}\overset{def}{=}inc(\cdot)_{ij}$. Then, Eq. (7) may be rewritten as

$$\mathbf{N}=inc(\mathbf{E}^e_I) \tag{8}$$

[4] In crystal plasticity, which we later relate to, $\mathbf{B}^p=\sum_\alpha\gamma^\alpha\mathbf{s}^\alpha\otimes\mathbf{m}^\alpha$ where γ^α is the plastic slip on slip system α comprising slip direction $\mathbf{s}^\alpha$ and slip normal $\mathbf{m}^\alpha$.

[5] Recently, Mesarovic et al. (2010) established the proof that for any strain field, there exists a unique orthogonal decomposition into compatible and incompatible strain fields.

[6] Henceforth, the subscripts C and I indicate the compatible and incompatible parts, respectively, of the kinematic quantities.

3.1. Compatibility of lattice curvature

Under general loading conditions not only will the strains be non-uniform (leading to a strain gradient), but the curvatures (i.e. first gradient of strain) may also vary between two material points. The corresponding tensor is referred to as the Nye tensor (Nye, 1953). In what follows, we systematically relate the incompatibility tensor **N** to the first gradient of the elastic part of the lattice curvature tensor.

The total lattice curvature tensor **K** is given as the gradient of the rotation vector $\mathbf{w}(=\frac{1}{2}\varepsilon_{ijk}W_{ij})$

$$K_{kl}=\tfrac{1}{2}\,\varepsilon_{ijk}W_{ij,l}=\tfrac{1}{2}\varepsilon_{ijk}u_{i,jl} \tag{9}$$

Noting that $\frac{1}{2}\varepsilon_{ijk}u_{l,ij}=0$, we obtain

$$K_{kl}=\tfrac{1}{2}\varepsilon_{ijk}(u_{i,lj}+u_{l,ij})=\varepsilon_{ijk}E_{il,j} \tag{10}$$

Again, in the presence of internal defects the total lattice curvature is still compatible; however, its elastic ($\mathbf{K}^e$) and plastic ($\mathbf{K}^p$) parts may individually be incompatible. The incompatible part of $\mathbf{K}^e$ is[7]

$$(\mathbf{K}_I^e)_{kl}=\varepsilon_{ijk}(\mathbf{E}_I^e)_{il,j} \tag{11}$$

The compatibility of the total lattice curvature tensor then gives[8]

$$curl(\mathbf{K}_I^e)=-curl(\mathbf{K}_I^p) \tag{12}$$

The compatible part of the curvature tensor $\mathbf{K}_C$ may be considered as the elastic lattice curvature due to the externally applied non-uniform stress, while the incompatible part of the curvature $\mathbf{K}_I$ is the additional lattice curvature due to the atomic misfit in the presence of GNDs. Further, $\mathbf{K}_I$ may be conceptually decomposed into their plastic ($\mathbf{K}_I^p$) and elastic ($\mathbf{K}_I^e$) parts. The plastic part is the lattice curvature arising due to the presence of GND density (Nye, 1953) while the incompatible elastic curvature tensor $\mathbf{K}_I^e$ is the additional lattice curvature that corresponds to the internal residual stress field due to the surrounding excess dislocation density. These different parts of the total lattice curvature may be explained by resorting to the two illustrations in Section 2. In the pure bending case, $\mathbf{K}_C^e$ and $\mathbf{K}_I^p$ represent the elastic lattice curvature and additional lattice curvature due to the presence of the GND density, respectively, while the $\mathbf{K}_I^e$ vanishes. However, in the non-uniform curvature example the lattice curvature due to the atomic misfit $\mathbf{K}_I$ includes both the elastic and plastic parts. Taking the curl of $\mathbf{K}_I^e$, we obtain

$$\begin{aligned}\varepsilon_{lmn}(K^e)_{kl,m} &= \varepsilon_{ijk}\varepsilon_{lmn}\,(E_I^e)_{il,jm}+\varepsilon_{ijk}\varepsilon_{lmn}\,(E_C^e)_{il,jm}\\ &= \varepsilon_{ijk}\varepsilon_{lmn}(E_I^e)_{il,jm}\end{aligned} \tag{13}$$

(the $(E_C^e)_{il,jm}$ term vanishes, as indicated)

Eq. (13) establishes that the gradient of the incompatible elastic curvature tensor is non-zero if a nonlinear strain (or stress) field exists due to an inhomogeneous GND density distribution in a given region.

3.2. Relation between incompatible elastic strain tensor and the GND density tensor

Nye (1953) defined the GND density tensor **A** whose components are related to the plastic part of the incompatible lattice curvature tensor

$$(K_I^p)_{kl}=A_{lk}-\tfrac{1}{2}\delta_{kl}A_{mm} \tag{14}$$

where $\mathbf{A}=curl(\mathbf{B}^p)=-curl(\mathbf{B}^e)$ and δ_{ij} is the Kronecker delta. Applying the curl operator to Eq. (14), we obtain

$$\varepsilon_{lmn}(K_I^p)_{kl,m}=\varepsilon_{lmn}A_{lk,m} \tag{15}$$

Noting the compatibility conditions for the curvature (see Eqs. (12) and (13)), we obtain the relation between the incompatible elastic strain and GND density tensors

$$\varepsilon_{lmn}A_{lk,m}=-\varepsilon_{ijk}\varepsilon_{lmn}(E_I^e)_{il,jm} \tag{16}$$

Since, the right hand side of Eq. (16) is symmetric we rewrite this equation by considering the symmetric part of the left hand side as well

$$N_{kn}=\varepsilon_{ijk}\varepsilon_{lmn}(E_I^e)_{il,jm}=-\tfrac{1}{2}(\varepsilon_{lmn}A_{lk,m}+\varepsilon_{lmk}A_{ln,m}) \tag{17}$$

Summarizing, we have established the relation between the gradient of the GND density tensor and the second gradient of the incompatible elastic strain tensor (Eq. (17)) in a continuum sense. This equation is central to deriving the expressions for the internal residual stress tensor, which is discussed in Section 4.

---

[7] Note that Eq. (11) may be equivalently written in terms of the incompatible parts of the plastic strain ($\mathbf{E}_I^p$) and curvature ($\mathbf{K}_I^p$) tensors.

[8] The compatibility condition for the curvature tensor is $curl(\mathbf{K})=0$. Then, $curl(\mathbf{K}^e+\mathbf{K}^p)=curl(\mathbf{K}_C^e+\mathbf{K}_I^e)+curl(\mathbf{K}_C^p+\mathbf{K}_I^p)=0\Rightarrow curl(\mathbf{K}_I^e)+curl(\mathbf{K}_I^p)=0$.

4. The internal residual stress tensor

In the preceding section, we introduced an incompatible elastic strain tensor $\mathbf{E}_I^e$ that is related to the GND density tensor (Eq. (17)). Corresponding to this strain tensor we introduce a work-conjugate internal stress tensor $\mathbf{T}^*$ via Hooke's law

$$\mathbf{T}^* = \mathbf{C} : \mathbf{E}_I^e \tag{18}$$

where $\mathbf{C}$ is the fourth-order elastic stiffness tensor for the bulk material. Then, using superposition, the total stress is

$$\mathbf{T} = \mathbf{C} : \mathbf{E}^e = \mathbf{C} : (\mathbf{E}_C^e + \mathbf{E}_I^e) = \underbrace{\mathbf{C} : \mathbf{E}_C^e}_{\mathbf{T}^{ext}} + \underbrace{\mathbf{C} : \mathbf{E}_I^e}_{\mathbf{T}^*} \tag{19}$$

Inverting Eq. (18) we rewrite Eq. (17) as

$$\varepsilon_{ijk}\varepsilon_{lmn}(S_{pqil}T^*_{pq})_{,jm} = -\tfrac{1}{2}(\varepsilon_{lmn}A_{lk,m} + \varepsilon_{lmk}A_{ln,m}) \tag{20}$$

where $\mathbf{S}(=\mathbf{C}^{-1})$ is the fourth-order compliance tensor.

Introduce a symmetric Beltrami stress function tensor $\boldsymbol{\varphi}$ (Sadd, 2005) to solve Eq. (20), such that[9]

$$T^*_{ij} = \varepsilon_{kni}\varepsilon_{lmj}\varphi_{kl,nm} = inc(\boldsymbol{\varphi}) \tag{21}$$

From Eqs. (8), and (21)

$$\mathbf{N} = inc(\mathbf{S} : inc(\boldsymbol{\varphi})) \tag{22}$$

i.e.

$$N_{kl} = \varepsilon_{ink}\varepsilon_{jml}(S_{ijpq}\varepsilon_{abp}\varepsilon_{cdq}(\varphi_{ab,cd}))_{,nm} \tag{23}$$

For an isotropic medium,[10] $\mathbf{S}$ depends only on the shear modulus μ and Poisson's ratio v. Then, Eq. (23) simplifies to (Kröner, 1959)

$$\mathbf{N} = \nabla^4\boldsymbol{\psi} \tag{24}$$

where

$$\psi_{kl} = \frac{1}{2\mu}\left(\varphi_{kl} - \frac{v}{1+2v}\varphi_{mm}\delta_{kl}\right) \tag{25}$$

A fully three-dimensional solution of Eq. (25) for an infinite medium is obtained using Green's function $G(\mathbf{r}-\mathbf{r}')$ (Kröner, 1959)

$$\boldsymbol{\psi}(\mathbf{r}) = \int_V G(|\mathbf{r}-\mathbf{r}'|)\mathbf{N}(\mathbf{r}')\,dV \tag{26}$$

$$G(|\mathbf{r}-\mathbf{r}'|) = -\frac{|\mathbf{r}-\mathbf{r}'|}{8\pi} \tag{27}$$

where G is the Green function that depends on the dimensionality of the problem and the elastic stiffness of the material (i.e. isotropic or anisotropic). Substituting $\mathbf{N}$ from Eq. (17), components of $\boldsymbol{\psi}$ are

$$\psi(\mathbf{r})_{kl} = \frac{1}{2}\varepsilon_{lmn}\int_V G(|\mathbf{r}-\mathbf{r}'|)A(\mathbf{r}')_{nk,m}\,dV + \frac{1}{2}\varepsilon_{kmn}\int_V G(|\mathbf{r}-\mathbf{r}'|)A(\mathbf{r}')_{nl,m}\,dV \tag{28}$$

Using the Green–Gauss theorem and setting the surface term at infinity equal to zero, Eq. (28) can be rewritten in the form

$$\psi(\mathbf{r})_{kl} = \frac{1}{2}\varepsilon_{mnl}\int_V G(|\mathbf{r}-\mathbf{r}'|)_{,m}A(\mathbf{r}')_{nk}\,dV + \frac{1}{2}\varepsilon_{mnk}\int_V G(|\mathbf{r}-\mathbf{r}'|)_{,m}A(\mathbf{r}')_{nl}\,dV \tag{29}$$

We assume appropriate boundary conditions (Groma et al., 2003; Mesarovic, 2005) when solving the BVPs so that the surface effects due to image dislocation fields may be neglected.

Inverting Eq. (25) and substitute it in Eq. (21), we obtain

$$T(\mathbf{r})^*_{ij} = \varepsilon_{kpi}\varepsilon_{lqj}\left[2\mu\left(\psi(\mathbf{r})_{kl,pq} + \frac{v}{1-v}\psi(\mathbf{r})_{mm,pq}\delta_{kl}\right)\right] \tag{30}$$

where

$$\psi(\mathbf{r})_{kl,pq} = \frac{1}{2}\varepsilon_{mnl}\int_V G(|\mathbf{r}-\mathbf{r}'|)_{,mpq}A(\mathbf{r}')_{nk}\,dV + \frac{1}{2}\varepsilon_{mnk}\int_V G(|\mathbf{r}-\mathbf{r}'|)_{,mpq}A(\mathbf{r}')_{nl}\,dV \tag{31}$$

[9] Eq. (21) satisfies stress equilibrium equation because $div(curl(curl(\cdot))) = 0$.

[10] The solutions for cubic symmetry and anisotropic cases are briefly discussed in Appendix B.

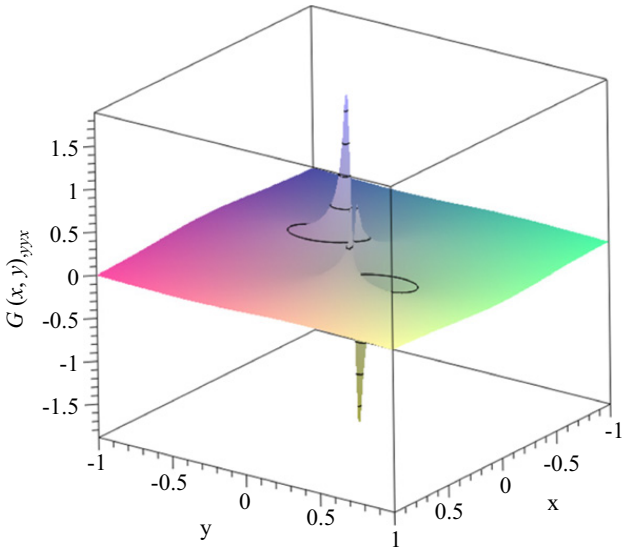

Fig. 3. Variation of a typical component of the third gradient of the Green function in Eq. (31).

Eq. (30) is the 3D constitutive law for the internal stresses, which can be solved analytically or numerically once the distribution of **A** is known. If Eq. (30) were to be integrated exactly over the whole continuum domain, it would mean that the stress field due to the GND density at each point influences the stress field at every other point in the body. However, it can be seen that Eq. (30), and consequently, the internal stress constitutive relation (Eq. (30)) are functions of the third gradient of G, which rapidly decays to zero (Fig. 3). Therefore, we may consider a small, but finite region (V') around a continuum point wherein the GND density distribution is accounted for (Evers et al., 2004; Gerken and Dawson, 2008; Groma, 1997; Mesarovic, 2005). Using the Taylor expansion of $\mathbf{A}(\mathbf{r}')$ around the point $\mathbf{r}$ in the region V' and assuming that only the first gradient of this series is important (Groma et al., 2003), we obtain

$$\psi(\mathbf{r})_{kl,pq} = \frac{1}{2}\varepsilon_{mnl}A(\mathbf{r})_{nk,r}\int_{V'}(x_r - x'_r)G(|\mathbf{r}-\mathbf{r}'|)_{,mpq}\,dV' + \frac{1}{2}\varepsilon_{mnk}A(\mathbf{r})_{nl,r}\int_{V'}(x_r - x'_r)G(|\mathbf{r}-\mathbf{r}'|)_{,mpq}\,dV' \tag{32}$$

The only parameter which remains to be chosen is the integration volume, V', which defines a length scale in the problem that gives nonlocal $\mathbf{T}^*$ (Eq. (30)). Note that $\mathbf{T}^*$does not depend on $\mathbf{A}$ at a continuum point, but only on its gradient. Using the crystallographic definition of $\mathbf{A} = \sum_\alpha(\nabla\gamma^\alpha \times \mathbf{m}^\alpha)\otimes\mathbf{s}^\alpha$, the resolved components of $\mathbf{T}^*$ on a slip system α are obtained as the function of Laplacian of the plastic slip γ^α. For a slip system α the contributions from other slip systems to its internal stress automatically enters the formulation.

4.1. Internal stress under plane strain condition:

Although the result obtained in the preceding section gives a 3D internal stress tensor (Eq. (30)) we explicitly write its components for the simpler case of plane strain. Assuming a plane strain condition in the z-direction, the only non-zero components of the GND density tensor (i.e. containing dislocation lines in the z-direction) are A_{xz}, A_{yz}, A_{zz}. Then, the non-zero components of incompatibility tensor are (see Eq. (17))

$$N_{zz} = -A_{zx,y} + A_{zy,x}; \quad N_{zx} = \tfrac{1}{2}A_{zz,y}; \quad N_{zy} = -\tfrac{1}{2}A_{zz,x} \tag{33}$$

From Eq. (21) the in-plane stresses can be obtained from the stress function tensor $\boldsymbol{\varphi}$

$$T^*_{xx} = \varphi_{zz,yy}; \quad T^*_{yy} = \varphi_{zz,xx}; \quad T^*_{xy} = -\varphi_{zz,xy} \tag{34}$$

where φ_{zz} is similar to an Airy stress function. The out-of-plane stresses are

$$T^*_{zx} = \varphi_{zx,yy} - \varphi_{zy,xy}; \quad T^*_{zy} = \varphi_{zy,xx} - \varphi_{zx,yx} \tag{35}$$

Eq. (24) can be solved in which $\psi_{zz} = ((1-\nu)/2\mu)\varphi_{zz}$ and then, the internal stress components are

$$T^*_{xx} = \frac{2\mu}{1-\nu}\left[A_{zy,x}\int_s x'G_{,y'y'x'}\,da' + A_{zy,y}\int_s y'G_{,y'y'x'}\,da' - A_{zx,x}\int_s x'G_{,y'y'y'}\,da' - A_{zx,y}\int_s y'G_{,y'y'y'}\,da'\right]$$
$$T^*_{yy} = \frac{2\mu}{1-\nu}\left[A_{zy,x}\int_s x'G_{,x'x'x'}\,da' + A_{zy,y}\int_s y'G_{,x'x'x'}\,da' - A_{zx,x}\int_s x'G_{,x'x'y'}\,da' - A_{zx,y}\int_s y'G_{,x'x'y'}\,da'\right]$$
$$T^*_{xy} = -\frac{2\mu}{1-\nu}\left[A_{zy,x}\int_s x'G_{,x'y'x'}\,da' + A_{zy,y}\int_s y'G_{,x'y'x'}\,da' - A_{zx,x}\int_s x'G_{,x'y'y'}\,da' - A_{zx,y}\int_s y'G_{,x'y'y'}\,da'\right] \tag{36a–c}$$

where S is the integration area that defines a length-scale. For the plane strain condition the appropriate Green function is (Kröner, 1959)

$$G(|\mathbf{r}-\mathbf{r}'|) = -\frac{(\mathbf{r}-\mathbf{r}')(\mathbf{r}-\mathbf{r}')}{8\pi}\ln(|\mathbf{r}-\mathbf{r}'|) \tag{37}$$

Choosing a square region $l_b \times l_b$ as the integration area, we obtain

$$\begin{aligned} T^*_{xx} &= \frac{2\mu}{1-\nu} l_b^2 \left[-0.068A_{zy,x} + 0.25A_{zx,y}\right] \\ T^*_{yy} &= \frac{2\mu}{1-\nu} l_b^2 \left[-0.25A_{zy,x} + 0.068A_{zx,y}\right] \\ T^*_{xy} &= -\frac{2\mu}{1-\nu} l_b^2 \left[-0.068A_{zy,y} + 0.068A_{zx,x}\right] \\ T^*_{zz} &= \nu(T^*_{xx} + T^*_{yy}) \end{aligned} \tag{38a–d}$$

where $T^*_{xx}, T^*_{yy}, T^*_{zz}$ and T^*_{xy} are the internal stress components due to edge dislocations, while those due to the screw components (T^*_{zx} and T^*_{zy}) are zero. When described in terms of the crystal plasticity framework the resolved internal shear stress $\tau^{*(\alpha)}$ due to Eqs. (38a–d) on αth slip system is, $\tau^{*(\alpha)} = \mathbf{s}^\alpha \cdot \mathbf{T}^* \mathbf{m}^\alpha$. These internal stresses bear close resemblance with those derived in the recent works Geers et al. (2007), Gerken and Dawson (2008) and Yefimov et al. (2004). Note that gradients in the dislocation densities may prevail in single crystal specimens due to a variety of reasons including geometric imperfections (Uchic et al., 2009), small misorientations, fabrication-induced defects (El-Awady et al., 2009b), etc. In polycrystalline materials, changes in crystal orientations across grain boundaries or twin boundaries may also set up regions with high GND density gradients in their vicinity. We highlight some of these aspects through the examples in Section 6.

The length-scale in this theory is mathematically necessary, but it must also be physically meaningful. Recently, Mesarovic et al. (2010) showed that a length-scale emerges from the thermodynamic coarsening error of the energies corresponding to the continuous and semi-discrete representations of stacked pile-ups, which is in the order of the average slip plane spacing ($\sim 100b$) for each slip system. Depending on the specific problem, microstructural length-scales may be related to, for example, average spacing of obstacles to dislocation motion in the form of grain boundaries (polycrystals), second-phase particles (heterogeneous alloys and composites), dislocation and cell-wall arrangements (single crystals). In other words, the length-scale has to be determined by the microstructural details and may be problem-dependent. One interpretation of the length-scale emerges from the comparison of Eqs. (39) with that of Yefimov et al. (2004) and relates to the average spacing of dislocations, i.e. $l_b \sim 1/\sqrt{\rho}$ (also see, Groma et al., 2003; Bayley et al., 2006). With this interpretation the internal length-scale may range between few tens of *nm* (very high dislocation density, e.g. Dao et al., 2006; Lu et al., 2009) to a few μm (low dislocation density, e.g. miniaturized single crystals) and the length-scale itself may evolve with deformation.

5. Principle of virtual power

In this section, we derive the equilibrium and constitutive equations for crystal plasticity including the internal stress using the purely mechanical version of the thermodynamic laws.

5.1. First law of thermodynamics: power balance

Given a virtual displacement field $\tilde{\boldsymbol{u}}$, the virtual external power of any sub-body of volume V bounded by surface S is

$$\tilde{P}_{\text{ext}} = \int_S \mathbf{t}(\mathbf{n}) \cdot \dot{\tilde{\boldsymbol{u}}}\, dS + \int_V \mathbf{f} \cdot \dot{\tilde{\boldsymbol{u}}}\, dV \tag{39}$$

where $\mathbf{t}(\mathbf{n})$ is the traction vector on a plane whose unit normal is $\mathbf{n}$ and $\mathbf{f}$ is the body force vector. The virtual internal power in the including the internal residual stress is

$$\tilde{P}_{int} = \int_V (\mathbf{T}^{ext} + \mathbf{T}^*) \cdot \nabla \dot{\tilde{\boldsymbol{u}}}\, dV \tag{40}$$

For any virtual displacement field, the internal and external powers should be balanced, so that

$$\int_S \mathbf{t}(\mathbf{n}) \cdot \dot{\tilde{\boldsymbol{u}}}\, dS + \int_V \mathbf{f} \cdot \dot{\tilde{\boldsymbol{u}}}\, dV = \int_V (\mathbf{T}^{ext} + \mathbf{T}^*) \cdot \nabla \dot{\tilde{\boldsymbol{u}}}\, dV \tag{41}$$

Using the divergence theorem, we obtain

$$\int_S (\mathbf{t}(\mathbf{n}) - (\mathbf{T}^{ext} + \mathbf{T}^*)\mathbf{n}) \cdot \dot{\tilde{\boldsymbol{u}}}\, dS + \int_V (div(\mathbf{T}^{ext} + \mathbf{T}^*) + \mathbf{f}) \cdot \dot{\tilde{\boldsymbol{u}}}\, dV = 0 \tag{42}$$

Since this equation should be valid for all sub-body V and any arbitrary virtual displacement $\tilde{\boldsymbol{u}}$, the nonlocal traction condition is

$$\mathbf{t}(\mathbf{n}) = (\mathbf{T}^{ext} + \mathbf{T}^*)\mathbf{n} \tag{43}$$

and the nonlocal force balance is

$$div(\mathbf{T}^{ext}+\mathbf{T}^{*})+\mathbf{f}=0 \tag{44}$$

Note that from Eq. (21), $div\,\mathbf{T}^{*}$ is always equal to zero. Then, Eq. (44) yields the classical force balance equation. Writing the plastic part of the total virtual displacement gradient vector in terms of the crystal plasticity framework, in the absence of any macroscopic motion, we have

$$\nabla\dot{\tilde{\boldsymbol{u}}}=\dot{\tilde{\mathbf{B}}}^{e}+\sum_{\alpha}\dot{\tilde{\gamma}}^{\alpha}(\mathbf{s}^{\alpha}\otimes\mathbf{m}^{\alpha})=\mathbf{0} \tag{45}$$

and the principle of virtual power (see Eq. (41)) yields

$$\int_{S}(\mathbf{t}^{*}(\mathbf{n})-(\mathbf{T}^{*})\mathbf{n})\cdot\dot{\tilde{\boldsymbol{u}}}\,dS=\int_{V}\left[(\mathbf{T}^{ext}+\mathbf{T}^{*})\cdot\dot{\tilde{\mathbf{B}}}^{e}+\sum_{\alpha}\tau^{\alpha}\cdot\dot{\tilde{\gamma}}^{\alpha}\right]dV \tag{46}$$

where τ^{α} is the total shear stress on slip system α. Using Eq. (45), we obtain[11]

$$-\tau^{\alpha}_{ext}-\tau^{*(\alpha)}+\tau^{\alpha}=0 \tag{47}$$

$$\mathbf{t}^{*}(\mathbf{n})=\mathbf{T}^{*}\cdot\mathbf{n} \tag{48}$$

where $\tau^{\alpha}_{ext}=\mathbf{s}^{\alpha}\cdot\mathbf{T}^{ext}\mathbf{m}^{\alpha}$ is the resolved shear stress due to external loads and $\mathbf{t}^{*}(\mathbf{n})$ is the microscopic traction vector.

5.2. Second law of thermodynamics: power imbalance

To derive the constitutive equation in the presence of the internal residual stress, we rewrite the second law of thermodynamics within the framework of crystal plasticity. The classical form of second law for isothermal condition is

$$\mathbf{T}:\dot{\mathbf{E}}-\dot{\psi}\geq 0 \tag{49}$$

where ψ is the free energy. Noting the orthogonal decomposition of the total strain tensor (Mesarovic et al., 2010), the total free energy may be decomposed as

$$\psi=\hat{\psi}(\mathbf{E}^{e}_{C})+\tilde{\psi}(\mathbf{E}^{e}_{I}) \tag{50}$$

where $\hat{\psi}$ is the standard elastic strain energy corresponding to the compatible part of the elastic strain tensor and $\tilde{\psi}$ is the defect energy that corresponds to the incompatible part of the elastic strain tensor. Substituting Eq. (50) in Eq. (49), we obtain

$$\left(\mathbf{T}^{ext}-\frac{\partial\hat{\psi}}{\partial\mathbf{E}^{e}_{C}}\right)\cdot\dot{\mathbf{E}}^{e}_{C}+\left(\mathbf{T}^{*}-\frac{\partial\tilde{\psi}}{\partial\mathbf{E}^{e}_{I}}\right)\cdot\dot{\mathbf{E}}^{e}_{I}+\sum_{\alpha}(\tau^{\alpha}_{ext}+\tau^{\alpha}_{*})\dot{\gamma}^{\alpha}\geq 0 \tag{51}$$

This inequality should hold for all choices of $\dot{\mathbf{E}}^{e}_{C}$, $\dot{\mathbf{E}}^{e}_{I}$ and $\dot{\gamma}^{\alpha}$; the linearity of this inequality in $\dot{\mathbf{E}}^{e}_{C}$ and $\dot{\mathbf{E}}^{e}_{I}$, respectively, provides the sufficient conditions for macroscopic and microscopic energetic constitutive equations

$$\mathbf{T}^{ext}=\frac{\partial\hat{\psi}}{\partial\mathbf{E}^{e}_{C}} \tag{52}$$

$$\mathbf{T}^{*}=\frac{\partial\tilde{\psi}}{\partial\mathbf{E}^{e}_{I}} \tag{53}$$

and from the inequality, we obtain

$$(\tau^{\alpha}_{ext}+\tau^{*(\alpha)})\dot{\gamma}^{\alpha}\geq 0 \tag{54}$$

A visco-plastic constitutive law satisfying the inequality in Eq. (54) can be written as

$$\dot{\gamma}^{\alpha}=\dot{\gamma}^{\alpha}_{0}\left|\frac{\tau^{\alpha}_{ext}+\tau^{*(\alpha)}}{g^{\alpha}_{T}}\right|^{n}sign(\tau^{\alpha}_{ext}+\tau^{*(\alpha)}) \tag{55}$$

where, $\dot{\gamma}^{\alpha}_{0}$ is the characteristic slip rate, n is the rate sensitivity index and g^{α}_{T} is the total crystallographic slip resistance due to the SSD density and the presence of the GND density (Han et al., 2005a, see Appendix A). Writing the total internal power and

[11] Eq. (48) is the same as the micro-force balance equation of Gurtin (2002) where $\tau^{*(\alpha)}=div\xi^{\alpha}$ where $\xi^{\alpha}$is the micro-stress vector. In the present approach the internal stress is work-conjugate to the incompatible elastic strain tensor, akin to Gurtin's defect stress (Gurtin, 2002) that work-conjugates with the GND density tensor.

comparing with the theory of Gurtin, et al. (2007) we identify the energetic and dissipative hardening terms

$$P_{\text{int}} = \int_V \left(\underbrace{\mathbf{T}^{ext} : \dot{\mathbf{E}}_C^e}_{\text{reversible stored power}} + \underbrace{\mathbf{T}^* : \dot{\mathbf{E}}_I^e}_{\text{irriversible stored power}} + \underbrace{\sum_\alpha (\tau_{ext}^\alpha + \tau^{*(\alpha)})\dot{\gamma}^\alpha}_{\text{dissipative power}} \right) dV \tag{56}$$

The first term in Eq. (56) represents the length-scale independent stress power (reversible stored power) associated with externally applied loads. The second term is referred to as the length-scale dependent energetic power (irreversible stored power) as it is associated with the internal residual stress and incompatible elastic strain that will tend to reorganize the GND density from an energetically efficient configuration. The third term in Eq. (56) is the plastic dissipation due to the SSD (length-scale independent) and GND (length-scale dependent) densities.

Tables 1–3 show key expressions developed in the present approach. Note that the internal stress tensor is blended into the continuum framework through ordinary equations of force balance and traction condition, and additional governing equations are not required.

6. Results and discussion

In this section, we investigate two problems involving single crystal specimens using the nonlocal visco-plastic constitutive relation (Eq. (55)). For simplicity we consider a two-dimensional plane strain setup with crystals oriented for symmetric double slip with respect to the loading direction.

6.1. Tapered single crystal specimen subjected to uniaxial loading

Fig. 4 shows a tapered single crystal of length L in plane strain condition that is constrained against slip at one end and subjected to an axial force F at the other end. The crystal is assumed to deform under symmetric double slip. The slip systems are oriented at an angle $\pm\theta$ giving

$$\begin{cases} s^1 = [\sin\theta, \cos\theta, 0], m^1 = [-\cos\theta, \sin\theta, 0] \\ s^2 = [-\sin\theta, \cos\theta, 0], m^2 = [-\cos\theta, -\sin\theta, 0] \end{cases}$$

Although this geometry is motivated by the recent micro-pillar experiments on single crystals, there are important differences that are discussed briefly before proceeding with the solution. First, the actual problem is essentially 3D, whereas we assume a plane strain condition. Further, as mentioned earlier, the present approach does not account for free surfaces

Table 1
Summary of governing equations.

Strain decomposition	$\mathbf{E}^e = \mathbf{E}_C^e + \mathbf{E}_I^e$
Kinematic relation	$\varepsilon_{ijk}\varepsilon_{lmn}(E_I^e)_{il,jm} = -\frac{1}{2}(\varepsilon_{lmn}A_{lk,m} + \varepsilon_{lmk}A_{ln,m})$
Local force balance	$div(\mathbf{T}^{ext}) + \mathbf{f} = 0$
Non-local force balance	$div(\mathbf{T}^*) = 0$

Table 2
Summary of constitutive equations.

Local elastic constitutive law	$\mathbf{T} = \mathbf{C} : \mathbf{E}_C^e$
Nonlocal internal stress constitutive law	$\mathbf{T}^* = \mathbf{C} : \mathbf{E}_I^e = \varepsilon_{kpi}\varepsilon_{lqj}\left[2\mu\left(\psi_{kl,pq} + \frac{\nu}{1-\nu}\psi_{mm,pq}\delta_{kl}\right)\right]$
Nonlocal visco-plastic constitutive law	$\dot{\gamma}^\alpha = \dot{\gamma}_0^\alpha \left\lvert \frac{\tau_{ext}^\alpha + \tau^{*(\alpha)}}{g_T^\alpha} \right\rvert^n sign(\tau_{ext}^\alpha + \tau_*^\alpha)$

Table 3
Summary of unknown variables and available equations.

Unknown parameters	No. of unknowns	Governing equations	No. of equations
$\mathbf{T}^{ext}$	6	$div(\mathbf{T}^{ext} + \mathbf{T}^*) = 0$	3
$\mathbf{E}^e$	6	$(\mathbf{T}^{ext} + \mathbf{T}^*) = \mathbf{C} : \mathbf{E}^e$	6
$\mathbf{E}^p$	6	$\mathbf{E}^p = E^p(\mathbf{T}^{ext}, \mathbf{T}^*, \ldots)$	6
$\mathbf{u}$	3	$\mathbf{E}^e + \mathbf{E}^p = (\nabla\mathbf{u})_{sym}$	6
$\mathbf{T}^*$	6	$\mathbf{T}^* = T^*(curl\,\mathbf{A}, \ldots)$	6
Total no.	27	Total no.	27

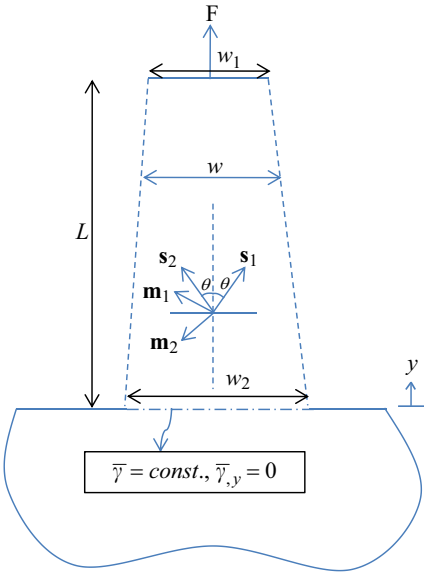

Fig. 4. A tapered bar under uniaxial loading. Dashed tapered edges indicate that they are sufficiently away from the centerline of the specimen.

that may give rise to image stresses and cause other mechanisms of strengthening. To circumvent the complexity associated with the free surface effects, we implicitly assume a quasi-1D situation in that the tapered boundaries are considered to be sufficiently away from the crystal center and their presence is accounted for only through the stress variation along its length from an applied force.[12]

We apply a uniaxial force F at the top and assume that at the base of the specimen ($y=0$), $\gamma^{\alpha}(0)=const$ (specifically, zero, in this example) and $\nabla\gamma^{\alpha}(0)=0$, so that the dislocations are free to move into the base, akin to a micro-pillar. The only non-vanishing stress component is then $\sigma_{yy}=F/w(y)$, where $w(y)$ is the width of the crystal at section y that changes linearly from w_1 at the loaded edge to w_2 at the constrained edge. Then, the resolved shear stress on each slip system is $\tau^{(1)}=-\tau^{(2)}=\sigma_{yy}\sin\theta\cos\theta$ and the corresponding plastic slip is $\gamma^1=-\gamma^2=\bar{\gamma}$. With the plastic strain tensor $\mathbf{E}^p=\sum_{\alpha}\gamma^{\alpha}(\mathbf{s}^{\alpha}\otimes\mathbf{m}^{\alpha})_{sym}$ the plastic slip gradient is $\nabla\bar{\gamma}=(0,\bar{\gamma}_{,y},0)$. In the crystallographic terms the GND density tensor is $\mathbf{A}=\sum_{\alpha}(\nabla\gamma^{\alpha}\times\mathbf{m}^{\alpha})\otimes\mathbf{s}^{\alpha}$; therefore, we obtain

$$\mathbf{A}=\begin{bmatrix}0 & 0 & 0\\ 0 & 0 & 0\\ 2cs\bar{\gamma}_{,y} & 0 & 0\end{bmatrix}$$

where c and s denote $\cos\theta$ and $\sin\theta$, respectively. For this problem the only non-zero GND density component is the one with the Burgers vector in the x-direction and the dislocation line in the z-direction. For the total slip hardening we adopt the SSD and GND dependent hardening of the form (Han et al., 2005b)

$$g^{\alpha}=g_0\left(\left(1+\frac{C_h}{g_0}|\bar{\gamma}^{\alpha}|\right)^2+l_g c|\bar{\gamma}_{,y}|\right)^{1/2} \tag{57}$$

The non-zero components of the internal stress tensor (see Eq. (38a–d)) are

$$\begin{aligned}T^*_{xx}&=\frac{\mu}{1-\nu}l_b^2 cs\bar{\gamma}_{,yy}\\ T^*_{yy}&=\frac{0.27\mu}{1-\nu}l_b^2 cs\bar{\gamma}_{,yy}\\ T^*_{zz}&=\nu(T^*_{xx}+T^*_{yy})\\ T^*_{xy}&=0\end{aligned} \tag{58}$$

and the corresponding resolved internal residual shear stress on each slip system is

$$(\tau^*)^1=-(\tau^*)^2=-Dl_b^2c^2s^2\bar{\gamma}_{,yy} \tag{59}$$

[12] Alternatively, one may assume that the tapered edges are coated (i.e. no free surface for the dislocation to exit the specimen) with a sufficiently thick material of elastic properties same as that of the crystal so that they do not pile up along those edges. These are obviously highly idealized assumptions, but enable us to consider a simpler system to provide semi-analytical solutions.

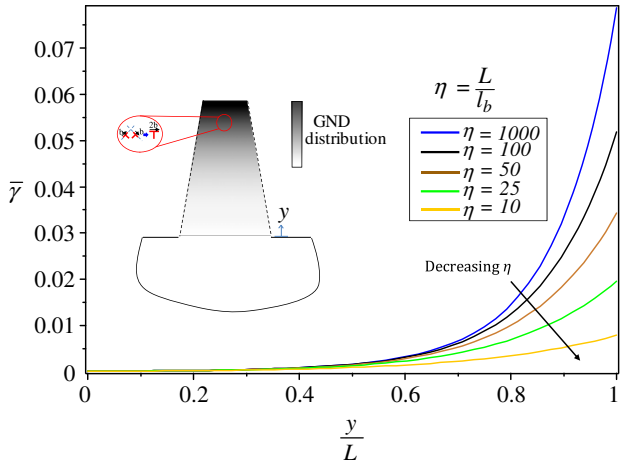

Fig. 5. Plastic slip $\bar{\gamma}$ along bar axis y for various ratio of $\eta = L/l_b$ for tapered specimen under monotonic tension.

where $=0.73\mu/(1-\nu)$. Substituting Eqs. (57) and (59) into Eq. (55) and integrating with respect to time, we obtain

$$\dot{\bar{\gamma}}^{\alpha} = \dot{\gamma}_0^{\alpha}\left|\frac{cs\frac{F}{w_2-((w_2-w_1)/L)y} - Dl_b^2c^2s^2\bar{\gamma}_{,yy}}{g_0\sqrt{(1+(C_h/g_0)|\bar{\gamma}^{\alpha}|)^2 + l_g c|\bar{\gamma}_{,y}|}}\right|^n sign(\tau_{tot}^{\alpha}) \tag{60}$$

Eq. (60) is solved using the fourth-order Runge–Kutta method. The material and geometric parameters used are $\dot{\gamma}_0^{\alpha} = 0.01$, $C_h = g_0/5$, $D = 1000g_0$, $\theta = \pm 45^{\circ}$, $w_1 = 0.2L$, $w_2 = 0.4L$ and $n = 10$. The results for monotonic and cyclic loading are discussed next.

6.1.1. *Monotonic loading*

To begin with, we investigate the influence of l_b by setting $l_g = 0$. Fig. 5 shows the variation of the magnitude of plastic slip along the length of the specimen for different $\eta = (L/l_b)$ ratios. As expected, the magnitude of the plastic slip decreases with decreasing η, that is for a smaller specimen size or larger l_b. With decreasing η the internal stress term in Eq. (60) becomes increasingly dominant and provides a strong resistance to the plastic slip. The increasing internal stress with decreasing η tends to homogenize the plastic slip as observed from the trend of the plastic slip variation with decreasing η.

Next, we highlight the relative influence of the two length-scale dependent dissipative hardening mechanisms, i.e. the dissipative hardening due to the presence of GND (corresponding to l_g) and the one due to GND density gradient (corresponding to l_b) on the overall response of the crystal. Figs. 6a and b show the normalized resolved shear stress on a slip system versus the magnitude of plastic slip at $y = L$ for different values of η and $\beta\,(=L/l_g)$ ratios. Fig. 6a shows that the length-scale dependent dissipative hardening due to the presence of GND influences the post-yield response, which has been previously reported by Han et al. (2005b) in the context of the MSG-CP theory. However, this enhanced hardening effect is discernable only when the slip is appreciably large, well beyond the initial yield. In comparison, Fig. 6b shows that the internal stress significantly influences both the response at incipient slip as well as at relatively larger slip. That is, the length-scale dependence due to the gradient of the GND density has a stronger influence on both the strengthening and hardening behavior of a crystal compared to that arising from the presence of the GND density. This is further exacerbated given that range of η ratios considered here is relatively smaller compared to the range of β ratios. Fig. 7 signifies the influence of geometric imperfection on the distribution of the internal stress along the specimen length. The larger the initial taper the more non-homogeneous is the GND density distribution that causes higher resolved internal shear stresses on individual slip systems. Consequently, the plastic slip on the slip systems would become harder giving an overall plastically stronger response.

The strong strengthening and hardening observed in this example is qualitatively similar to the specimen length-scale dependent strengthening behaviors reported in some of the recent experiments on miniaturized single crystals (e.g. Frick et al., 2008) that indicate presence of the GND density. While the actual mechanisms of strengthening in such miniaturized experiments have not been fully unraveled, the results from the present work correlate qualitatively with the experimentally observed size-dependent plasticity in the presence of strong gradients (Maaß et al., 2006). Although in the present case the gradient in the GND density is due to specimen taper, presence of fillets, low angle boundaries (Uchic et al., 2009) or surface damage layers due to fabrication may also produce significant gradients at small specimen sizes (El-Awady et al., 2009b). Thus, the non-gradient based size-effects (e.g. source-limited dislocation plasticity and dislocation starvation) postulated in such experiments may be augmented by those due the internal stresses arising from the non-homogeneous distribution of the GND density.

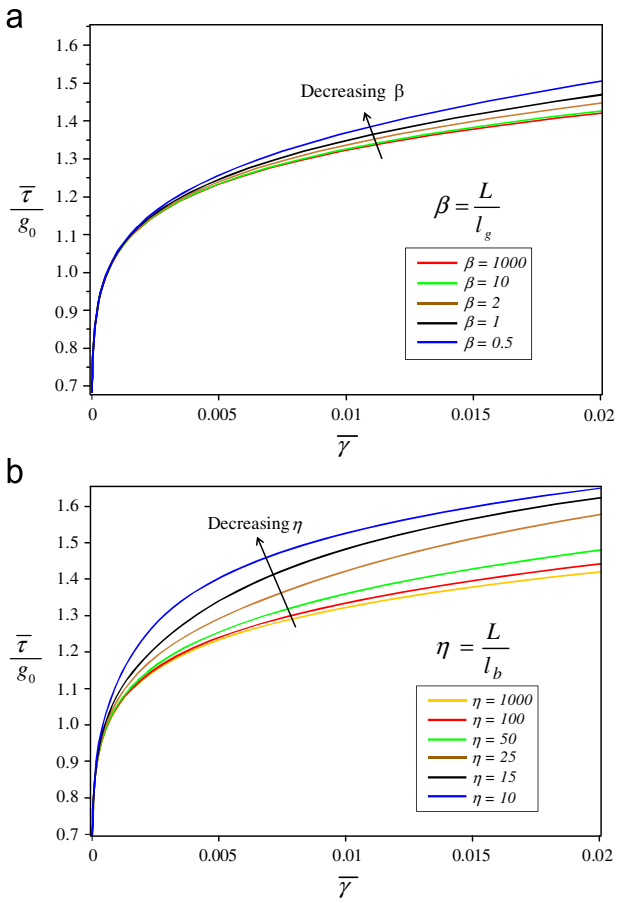

Fig. 6. Resolved shear stress versus plastic slip at $y = L$ for tapered bar under monotonic tension for various ratios (a) $\beta = L/l_g$ and (b) $\eta = L/l_b$.

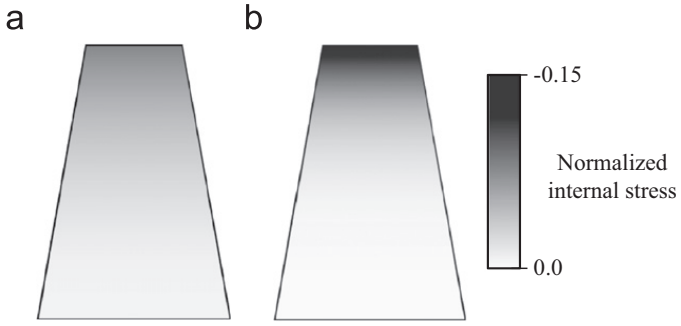

Fig. 7. Distribution of normalized internal shear stress ($\overline{\tau}^*/\overline{\tau}$) along the tapered specimen under monotonic tension for (a) $\lambda = 2.86^\circ$ and (b) $\lambda = 5.71^\circ$. $\eta = 50$.

6.1.2. *Cyclic loading*

We now investigate the response of the tapered single crystal specimen under a single tension–compression cycle. Many metals exhibit the well-known Bauschinger effect under cyclic loading. In the present work, the internal stress tensor derived from the inhomogeneous GND density distribution produces a size-dependent Bauschinger effect. For simplicity, we suppress the contribution from the dissipative hardening by setting $l_g = 0$.

Fig. 8 shows the resolved shear stress versus plastic slip curves at $y = L$ plotted for two different values of η. We also include the response of the same specimens under monotonic loading. For fixed η the monotonic compressive response is much stronger than if the specimen were loaded under a single tension–compression cycle. The disparity between the monotonic and cyclic responses increases with decreasing η giving a length-scale dependent Bauschinger effect (Kiener et al., 2010; Xiang and Vlassak, 2006). The enhanced strengthening and hardening during the initial tensile loading is because the internal residual stress opposes the applied stress. However, upon reverse loading the direction of the resolved shear stress due to external load reverses, but that of the internal stress does not as the GND arrangement is unaffected. This causes the specimen to yield at a smaller load in the reverse loading. The hardening behavior is also weaker in the reverse loading compared to the initial forward response. In a realistic scenario with more than two slip systems, one may observe stronger hardening because of latent hardening that may accentuate the Bauschinger effect (Bayley et al., 2006). Fig. 9 shows that geometric imperfections

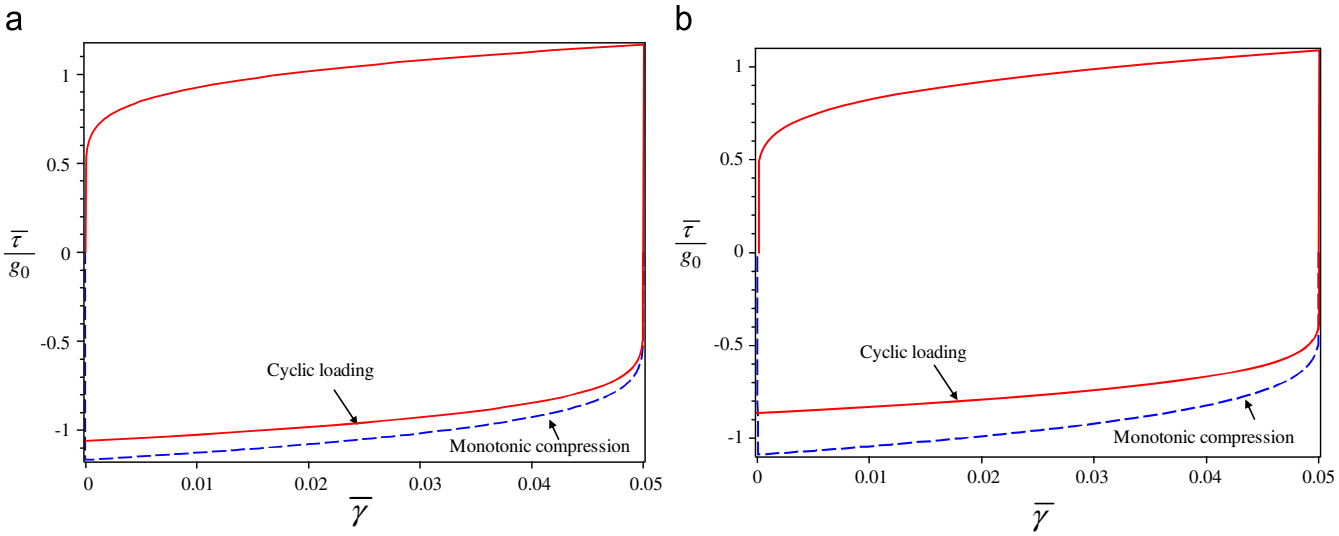

Fig. 8. Resolved shear stress versus plastic slip at $y=L$ for tapered bar under cyclic loading (a) $\eta=100$ and (b) $\eta=50$.

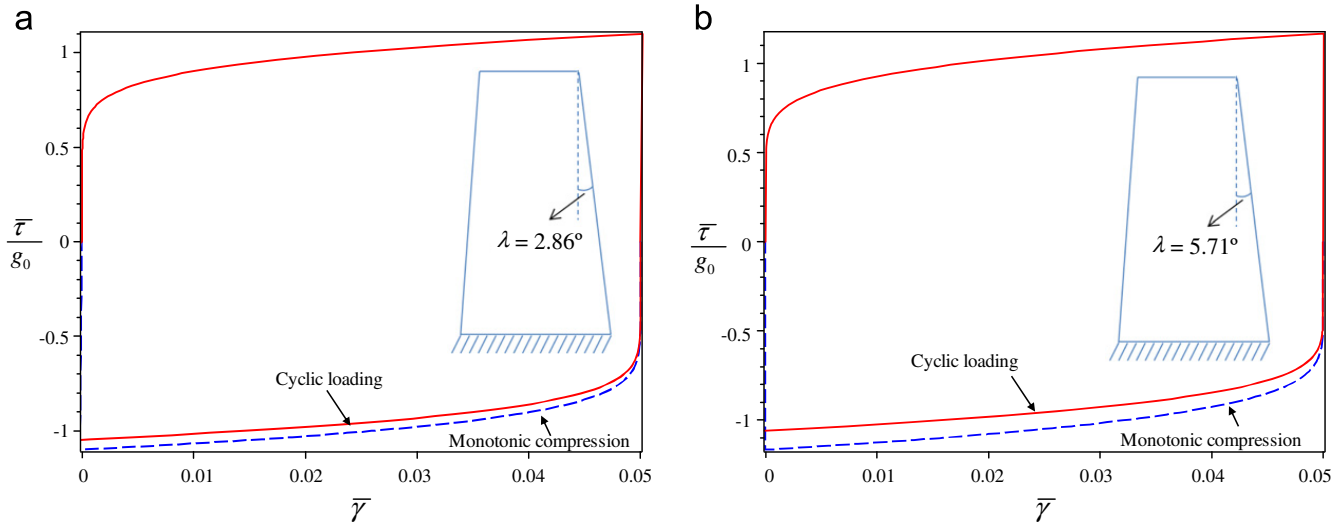

Fig. 9. Resolved shear stress versus plastic slip at $y=L$ for various tapered angles under cyclic loading ($\eta=100$) (a) $\lambda=2.86^\circ$ and (b) $\lambda=5.71^\circ$.

strongly influence the Bauschinger effect and it increases with increasing degree of imperfection. Such an asymmetric response cannot be predicted solely by a theory that does not account for the effect of distribution of the dislocation density. This is true irrespective of the particular nature of the strain gradient theory (Xiang and Vlassak, 2006).

6.2. *Single crystal lamella subjected to simple shear*

In the previous problem, the internal stress appeared because of non-homogeneous distribution of the stress due to geometric imperfections. Here, we consider the internal stress in a specimen with no geometric non-uniformities, but due to the pile-up of dislocations at impenetrable boundaries. Consider a layered crystal as shown in Fig. 10. We isolate a single layer from this crystal and assume it to be a semi-infinite lamella of thickness 2λ with symmetric double planar slip subjected to simple shear. This geometry is reflective of a typical twin lamella within a grain of a nano-twinned polycrystal (Lu et al., 2009). We consider hard boundary conditions on the lamella boundaries such that

$$\gamma^{\alpha}(0)=0, \quad \gamma^{\alpha}(2\lambda)=0; \quad \alpha=1,2 \tag{61}$$

These conditions ensure that no plastic slip occurs along a slip system at the boundaries causing dislocations to pile up there. The only non-zero component of macroscopic stress in this problem is T_{yx}. The corresponding resolved shear stress and plastic slip due to the external load are, respectively, $\tau^1=-\tau^2=\overline{\tau}=T_{yx}\cos 2\theta$ and $\gamma^1=-\gamma^2=\overline{\gamma}$, where θ is the orientation of the slip systems with respect to the loading direction. The plastic slip gradient is $\nabla\overline{\gamma}=(0,\overline{\gamma}_{,y},0)$ and the continuum dislocation

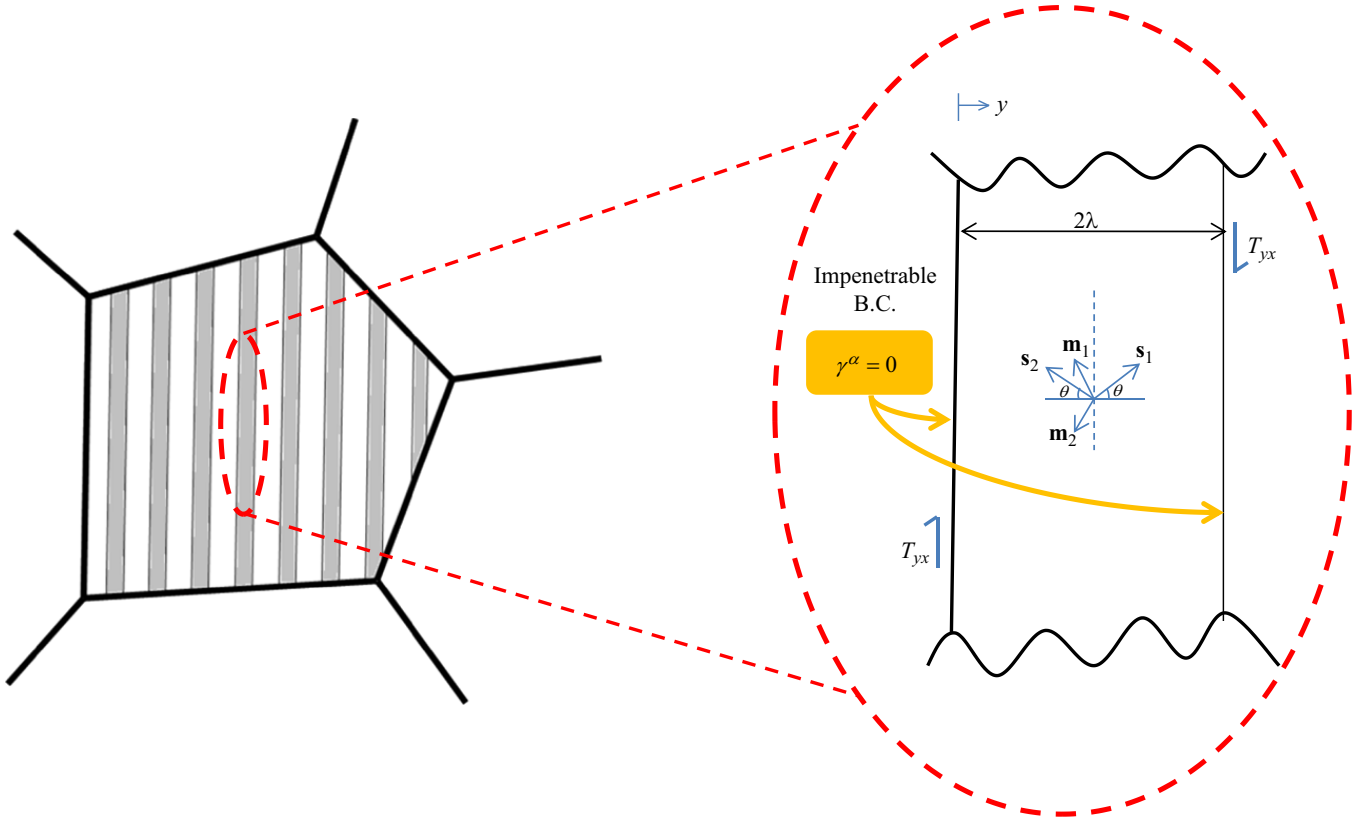

Fig. 10. A single lamella within a nano-twinned crystal under simple shear.

density tensor **A** for this case is

$$\mathbf{A}=\begin{bmatrix}0 & 0 & 0\\ 0 & 0 & 0\\ 0 & -2s^2\overline{\gamma}_{,y} & 0\end{bmatrix}$$

From Eq. (38a–d) and using the Schmid law, the resolved internal shear stress on each slip system is

$$(\tau^*)^1=-(\tau^*)^2=\overline{\tau}^*=-\frac{0.136\mu}{1-\nu}l_b^2s^2\overline{\gamma}_{,yy}\cos 2\theta \tag{62}$$

and the corresponding plastic slip is

$$\overline{\gamma}^{\alpha}=\gamma_0^{\alpha}\left|\frac{(T_{yx}-(0.136\mu/(1-\nu))l_b^2s^2\overline{\gamma}_{,yy})\cos 2\theta}{g_0\sqrt{(1+(C_h/g_0)|\overline{\gamma}^{\alpha}|)^2+l_gc|\overline{\gamma}_{,y}|}}\right|^n sign(\tau_{tot}^{\alpha}) \tag{63}$$

The material parameters are the same as in the previous example, except θ, which is set equal to 90° providing the highest plastic incompatibility. Fig. 11a shows the normalized resolved shear stress-average plastic slip response for different $\eta=\lambda/l_b$. As expected, strong strengthening occurs by decreasing η. Fig. 11b shows the normalized resolved shear stress at $\overline{\gamma}=0.002$ as a function of normalized lamella thickness. It is interesting to note that for the range of η values shown in the figure the strengthening trend compares well with Hall–Petch behavior.

For a given applied stress, Eq. (63) plastic slip variation along the lamella thickness can be obtained, subject to the boundary conditions in Eq. (61). For fixed applied loading ($T_{yx}=1.5g_0$), Figs. 12a and b, respectively, show the variation of plastic slip and normalized internal resolved shear stress on a slip system along the normalized thickness ordinate for different values of η. As shown in these figures, for fixed l_b (i.e. same material), when the lamella thickness is much larger compared to the internal length-scale ($\eta\gg 1$), only a very narrow region is affected by the boundary and away from it the effect decays rapidly. The plastic slip away from the boundary reaches a constant value (Fig. 12a), which corresponds to the absence of internal stress in that region (Fig. 12b). However, as the lamella thickness approaches the internal length-scale ($\eta\to 1$) the *boundary affected zone (b.a.z.)* occupies a significant portion of the lamella. The magnitude of internal stress over the lamella thickness increases and at the same time it becomes more diffuse, i.e. it extends over the entire lamellar region. Correspondingly, it becomes increasingly difficult to produce plastic slip. With even further decrease in the lamella thickness ($\eta<1$) the internal stress distribution within the lamella becomes nearly uniform (except at the boundary) and its magnitude

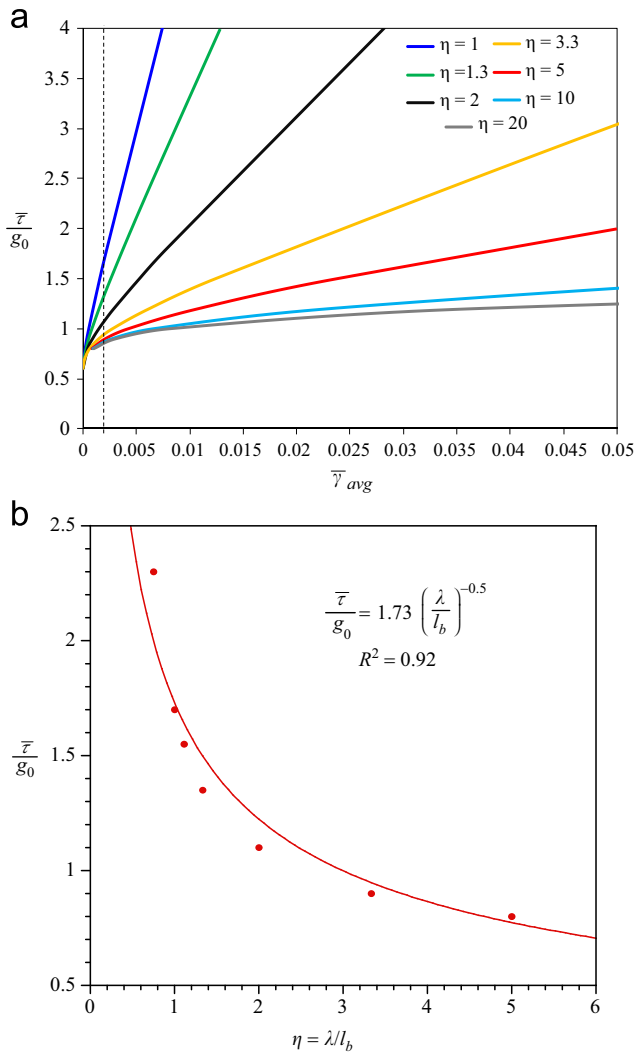

Fig. 11. (a) Normalized resolved shear stress ($\overline{\tau}/g_0$) versus average plastic slip as a function of η for $\theta = 90^\circ$ and (b) normalized resolved shear stress ($\overline{\tau}/g_0$) versus normalized lamella thickness at $\overline{\gamma} = 0.2\%$.

tends to saturate. Fig. 12c captures this aspect clearly in that it shows an initial strong increase in the normalized internal resolved shear stress as η decreases, but a tendency to saturate at very small η. Although not shown in Fig. 11b, the corresponding slip system strengthening also tends to saturate with the saturation of the internal residual shear stress.

7. Summary

In this paper, we developed a nonlocal crystal plasticity approach enriched by internal residual stresses that arise due to the non-homogeneous distribution of GND densities. The salient feature of this work is the analytical derivation of the length-scale dependent 3D internal stress tensor using the stress function approach. This second order internal stress tensor blends into the conventional equilibrium equations. In the crystal plasticity framework, the internal stresses appear as additional resolved shear stresses on each slip system alongside those due to the externally applied loads. The visco-plastic constitutive law for crystallographic slip that includes this effect is presented in a thermodynamically consistent manner. The connections between the continuum and crystallographic variables in this formulation render it useful for the development of computational framework for the J_2-deformation theory as well as the small strain crystal plasticity theory.

The analytical examples highlight the importance of the internal stress on the size-dependent strengthening and hardening in single crystals. Geometric imperfections can cause strong gradients in the GND density and lead to a strengthening of the overall stress–strain response in specimens that are subjected to nominally uniaxial macroscopic loads. As evident from the second example, the internal stress-induced strengthening of a slip system is akin to the Hall–Petch behavior, but tends to saturate at small microstructural sizes.

As a closure, we briefly compare the present approach with some of the existing nonlocal theories that incorporate the internal residual stresses. The key equations derived here for internal stresses results bear close resemblance with the pioneering efforts of Groma and co-workers that use a statistical approach mimicking the collective behavior of dislocations (Groma and Bakó, 1998;

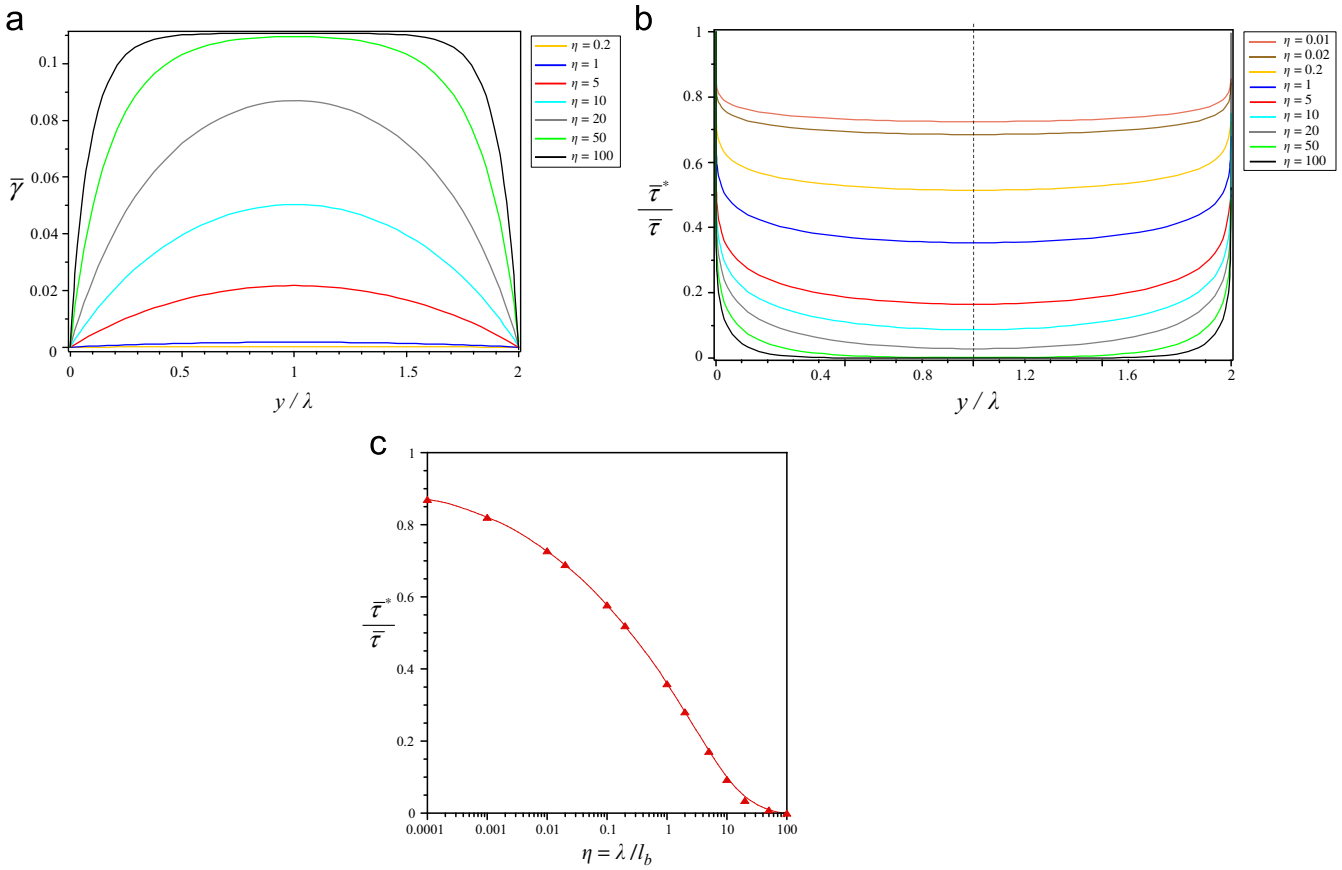

Fig. 12. (a) Distribution of plastic slip ($\bar{\gamma}$) on a slip system as a function of η for $\theta = 90^\circ$ versus distance normalized by lamella thickness λ, (b) normalized internal resolved shear stress ($\bar{\tau}^*/\bar{\tau}$) along the lamella thickness as a function of η for θ=90° and (c) normalized internal resolved shear stress ($\bar{\tau}^*/\bar{\tau}$) versus normalized lamella thickness.

Groma et al., 2003; Zaiser et al., 2001). Recent versions of this approach by Yefimov et al. (2004) have been developed for edge dislocations. The approach of Gerken and Dawson (2008) again restricts its focus on the internal stresses due to edge dislocations. In their theory, the average internal stress fields derived from Volterra dislocations are simplified assuming a bilinear variation of the GND density, but the motivation behind this choice is not obvious. Recently, Ertürk et al. (2009) presented a sophisticated crystal plasticity approach with back stresses accounting for the latent hardening effects due to both screw and edge GNDs. In comparison to these approaches, the present approach is based on a continuum theory of kinematic coarsening and also includes contributions from edge and screw components of the GNDs. The projection of the gradient of the GND density tensor on to a given slip system leads to the contribution from other slip systems providing a latent hardening effect. Further, it should be possible to extend this approach to anisotropic elastic cases using appropriate stress functions (Appendix B). This aspect seems not well-outlined in most theories in that the development is restricted to elastically isotropic cases.

Our on-going work focuses on implementing this approach in a finite element framework and investigating the strengthening and hardening behaviors of heterogeneous polycrystalline systems.

Acknowledgements

SPJ acknowledges partial financial support from NUS-AcRF-Tier 1 Grant # R-265-000-294-133, and JNR acknowledges the support through Oscar S Waytt Endowed Chair. SPJ and RA acknowledge fruitful discussions with R. Narasimhan (IISc, Bangalore).

Appendix A. Plastic-slip gradient induced dissipative hardening

Using the formulation derived by Han et al. (2005a), the total slip-induced hardening on an αth slip system is

$$g_T^\alpha = g_0 \sqrt{\left(\frac{g_{SSD}^\alpha}{g_0}\right)^2 + l_g \chi_G^\alpha} \tag{A1}$$

where g_0 is the initial lattice resistance, g^{α}_{SSD} is the conventional hardening due to the statistically stored dislocation (SSD) density ρ^{α}_{SSD}

$$g^{\alpha}_{SSD} = a\mu b\sqrt{\rho^{\alpha}_{SSD}} \tag{A2}$$

Here b is the magnitude of Burgers vector, a is the Taylor coefficient that empirically embeds the information related to dislocation distribution, crystal orientation, temperature, etc. The length-scale dependent hardening in Eq. (A1) is related to the effective dislocation density

$$\chi^{\alpha}_{G} = \left| \mathbf{m}^{\alpha} \times \sum_{\beta} s^{\alpha\beta} \nabla\gamma^{\beta} \times \mathbf{m}^{\beta} \right| \tag{A3}$$

where $s^{\alpha\beta} = \mathbf{s}^{\alpha} \cdot \mathbf{s}^{\beta}$, $l_g = a^2\mu^2 b/g_0^2$ and $\nabla\gamma^{\beta}$ is the plastic slip gradient on the slip system β

$$\nabla\gamma^{\beta} = \gamma^{\beta}_{,m}\mathbf{m}^{\beta} + \gamma^{\beta}_{,s}\mathbf{s}^{\beta} + \gamma^{\beta}_{,t}\mathbf{t}^{\beta} \tag{A4}$$

and $\mathbf{t}^{\beta} = \mathbf{m}^{\beta} \times \mathbf{s}^{\beta}$.

Appendix B. Stress function approach for elastic anisotropy

In Section 4, we derived the internal residual stress using Beltrami stress function for an elastically isotropic material. Here, the extension for anisotropic case is presented (Kröner, 1955). For the anisotropic case the incompatibility equation is written as (compare Eq. (22))

$$f(\nabla)\boldsymbol{\psi} = \mathbf{N} \tag{B1}$$

where $\boldsymbol{\psi}$ is fourth-order stress function tensor and $f(\nabla)$ is a scalar sixth-order differential operator which is given by

$$f(\nabla) = \varepsilon_{lpq}\varepsilon_{mrs} D_{lm}(\nabla) \cdot D_{pr}(\nabla) \cdot D_{qs}(\nabla) \tag{B2}$$

In Eq. (B2) $D_{ik} = C_{ijkl}(\cdot)_{jl}$ is a second order tensor operator with C_{ijkl} as the elastic constant. The Green function solution of Eq. (B1) is given by (compare Eq. (36))

$$\boldsymbol{\psi}(\mathbf{r}) = \int_V G(|\mathbf{r}-\mathbf{r}'|)\mathbf{N}(\mathbf{r}')dV \tag{B3}$$

where G is the appropriate Green function for the anisotropic case. For cubic symmetry, the Green function is (Burgers, 1939; Kröner, 1953)

$$G(|\mathbf{r}-\mathbf{r}'|) = a \cdot (|\mathbf{r}-\mathbf{r}'|^3), \quad a = C_{11}C_{44}^2/96\pi \tag{B4}$$

Further studies for the anisotropic cases can be found in the works of Leutz and Bauer (1976) and Steeds and Willis (1979). Then, the internal stress $\mathbf{T}^*$ is given by Eq. (21) where the relation between Beltrami stress function tensor $\boldsymbol{\varphi}$ and fourth-order stress function tensor $\boldsymbol{\psi}$ is defined using a second-order differential operator X_{ijkl} as

$$\varphi_{kl} = X_{ijkl}\psi_{kl} \tag{B5}$$

The explicit formulation for X_{ijkl} operator for cubic symmetry media has been derived by Kröner (1955) and extended to fully anisotropic case by Michelitsch and Wunderlin (1996).

References

Abu Al-Rub, R.K., Voyiadjis, G.Z., Bammann, D.J., 2007. A thermodynamic based higher-order gradient theory for size dependent plasticity. International Journal of Solids and Structures 44 (9), 2888–2923.

Acharya, A., Bassani, J.L., 2000. Lattice incompatibility and a gradient theory of crystal plasticity. Journal of the Mechanics and Physics of Solids 48 (8), 1565–1595.

Acharya, A., Roy, A., 2006. Size effects and idealized dislocation microstructure at small scales: predictions of a phenomenological model of mesoscopic field dislocation mechanics: Part I. Journal of the Mechanics and Physics of Solids 54 (8), 1687–1710.

Aifantis, E.C., 1984. On the microstructural origin of certain inelastic models. Journal of Engineering Materials and Technology 106 (4), 326–330.

Aifantis, E.C., 1999. Strain gradient interpretation of size effects. International Journal of Fracture 95 (1–4), 299–314.

Bardella, L., 2006. A deformation theory of strain gradient crystal plasticity that accounts for geometrically necessary dislocations. Journal of the Mechanics and Physics of Solids 54 (1), 128–160.

Bardella, L., 2007. Some remarks on the strain gradient crystal plasticity modelling, with particular reference to the material length scales involved. International Journal of Plasticity 23 (2), 296–322.

Bayley, C.J., Brekelmans, W.A.M., Geers, M.G.D., 2006. A comparison of dislocation induced back stress in strain gradient crystal plasticity. International Journal of Solids and Structures 43, 7268–7286.

Bazant, Z.P., Pijaudier-Cabot, G., 1988. Nonlocal continuum damage, localization instability and convergence. Journal of Applied Mechanics 55, 287–293.

Burgers, J.M., 1939. Proc. Kon. Nederl. Akad. Wetensch 42, 293,378.

Dao, M., Lu, L., Shen, Y.F., Suresh, S., 2006. Strength, strain-rate sensitivity and ductility of copper with nanoscale twins. Acta Materialia 54 (20), 5421–5432.

Dehm, G., 2009. Miniaturized single-crystalline fcc metals deformed in tension: new insights in size-dependent plasticity. Progress in Materials Science 54 (6), 664–688.

El-Awady, J.A., Wen, M., Ghoniem, N.M., 2009a. The role of the weakest-link mechanism in controlling the plasticity of micropillars. Journal of the Mechanics and Physics of Solids 57 (1), 32–50.

El-Awady, J.A., Woodward, C., Dimiduk, D.M., Ghoniem, N.M., 2009b. Effects of focused ion beam induced damage on the plasticity of micropillars. Physical Review B—Condensed Matter and Materials Physics 80, 10.
Eringen, A.C., 1983. On differential equations of nonlocal elasticity and solutions of screw dislocation and surface waves. Journal of Applied Physics 54 (9), 4703–4710.
Ertürk, I., Van Dommelen, J.A.W., Geers, M.G.D., 2009. Energetic dislocation interactions and thermodynamical aspects of strain gradient crystal plasticity theories. Journal of the Mechanics and Physics of Solids 57 (11), 1801–1814.
Evans, A.G., Hutchinson, J.W., 2009. A critical assessment of theories of strain gradient plasticity. Acta Materialia 57 (5), 1675–1688.
Evers, L.P., Brekelmans, W.A.M., Geers, M.G.D., 2004. Non-local crystal plasticity model with intrinsic SSD and GND effects. Journal of the Mechanics and Physics of Solids 52 (10), 2379–2401.
Fleck, N.A., Hutchinson, J.W., 1993. A phenomenological theory for strain gradient effects in plasticity. Journal of the Mechanics and Physics of Solids 41 (12), 1825–1857.
Frick, C.P., Clark, B.G., Orso, S., Schneider, A.S., Arzt, E., 2008. Size effect on strength and strain hardening of small-scale [1 1 1] nickel compression pillars. Materials Science and Engineering A 489 (1-2), 319–329.
Gao, H., Huang, Y., Nix, W.D., Hutchinson, J.W., 1999. Mechanism-based strain gradient plasticity—I. Theory. Journal of the Mechanics and Physics of Solids 47 (6), 1239–1263.
Geers, M.G.D., Brekelmans, W.A.M., Bayley, C.J., 2007. Second-order crystal plasticity: Internal stress effects and cyclic loading. Modelling and Simulation in Materials Science and Engineering 15 (1), S133–S145.
Gerken, J.M., Dawson, P.R., 2008. A crystal plasticity model that incorporates stresses and strains due to slip gradients. Journal of the Mechanics and Physics of Solids 56 (4), 1651–1672.
Groma, I., 1997. Link between the microscopic and mesoscopic length-scale description of the collective behavior of dislocations. Physical Review B—Condensed Matter and Materials Physics 56 (10), 5807–5813.
Groma, I., Bako´, B¨, 1998¨ Probability distribution of internal stresses in parallel straight dislocation systems. Physical Review B—Condensed Matter and Materials Physics 58 (6), 2969–2974.
Groma, I., Csikor, F.F., Zaiser, M., 2003. Spatial correlations and higher-order gradient terms in a continuum description of dislocation dynamics. Acta Materialia 51 (5), 1271–1281.
Gurtin, M.E., 2000. On the plasticity of single crystals: free energy, microforces, plastic-strain gradients. Journal of the Mechanics and Physics of Solids 48 (5), 989–1036.
Gurtin, M.E., 2002. A gradient theory of single-crystal viscoplasticity that accounts for geometrically necessary dislocations. Journal of the Mechanics and Physics of Solids 50 (1), 5–32.
Gurtin, M.E., Anand, L., 2007. A gradient theory for single-crystal plasticity. Modelling and Simulation in Materials Science and Engineering 15, 1.
Han, C.S., Gao, H.J., Huang, Y., Nix, W.D., 2005a. Mechanism-based strain gradient crystal plasticity—I. Theory. Journal of the Mechanics and Physics of Solids 53, 1188–1203.
Han, C.S., Gao, H.J., Huang, Y., Nix, W.D., 2005b. Mechanism-based strain gradient crystal plasticity—II. Analysis. Journal of the Mechanics and Physics of Solids 53, 1204–1222.
Huang, Y., Qu, S., Hwang, K.C., Li, M., Gao, H., 2004. A conventional theory of mechanism-based strain gradient plasticity. International Journal of Plasticity 20 (4–5), 753–782.
Kiener, D., Motz, C., Grosinger, W., Weygand, D., Pippan, R., 2010. Cyclic response of copper single crystal micro-beams. Scripta Materialia 63 (5), 500–503.
Kröner, E., 1953. Das Fundamentalintegral der anisotropen elastischen Differentialgleichungen. Zeitschrift fur Physik 136, 402–410.
Kröner, E., 1955. Die Spannungsfunktionen der dreidiminsionalan anisotropen Elastizitatstheorie. Zeitschrift fur Physik 141, 386.
Kröner, E., 1959. Allgemeine Kontinuumstheorie der Versetzungen und Eigenspannungen. Archive for Rational Mechanics and Analysis 4 (Suppl. 1), 273–334.
Kuroda, M., Tvergaard, V., 2006. Studies of scale dependent crystal viscoplasticity models. Journal of the Mechanics and Physics of Solids 54 (9), 1789–1810.
Kuroda, M., Tvergaard, V., 2008a. A finite deformation theory of higher-order gradient crystal plasticity. Journal of the Mechanics and Physics of Solids 56 (8), 2573–2584.
Kuroda, M., Tvergaard, V., 2008b. On the formulations of higher-order strain gradient crystal plasticity models. Journal of the Mechanics and Physics of Solids 56 (4), 1591–1608.
Leutz, R.K., Bauer, R., 1976. Computation of the anisotropic cubic elastic green's tensor function and the elastic energy coefficients of point defects in crystals. Computer Physics Communications 11 (3), 339–351.
Lu, L., Chen, X., Huang, X., Lu, K., 2009. Revealing the maximum strength in nanotwinned copper. Science 323 (5914), 607–610.
Mesarovic, S.D., 2005. Energy, configurational forces and characteristic lengths associated with the continuum description of geometrically necessary dislocations. International Journal of Plasticity 21 (10), 1855–1889.
Mesarovic, S.D., Baskaran, R., Panchenko, A., 2010. Thermodynamic coarsening of dislocation mechanics and the size-dependent continuum crystal plasticity. Journal of the Mechanics and Physics of Solids 58 (3), 311–329.
Michelitsch, T., Wunderlin, A., 1996. Stress function and internal stress in linear three-dimensional anisotropic elasticity. Zeitschrift fur Physik 100, 53–56.
Nix, W.D., Gao, H., 1998. Indentation size effects in crystalline materials: A law for strain gradient plasticity. Journal of the Mechanics and Physics of Solids 46 (3), 411–425.
Nye, J.F., 1953. Some geometrical relations in dislocated crystals. Acta Metallurgica 1 (2), 153–162.
Sadd, M.H., 2005. Elasticity—Theory, Applications and Numerics. Elsevier Butterworth-Heinemann, New York.
Shu, J.Y., Fleck, N.A., Van Der Giessen, E., Needleman, A., 2001. Boundary layers in constrained plastic flow: comparison of nonlocal and discrete dislocation plasticity. Journal of the Mechanics and Physics of Solids 49 (6), 1361–1395.
Steeds, J.W., Willis, J.R., 1979. In: Nabarro, F.R.N. (Ed.), Dislocations in Anisotropic Media in Dislocations in Solids, vol. 1. North-Holland, Amsterdam.
Uchic, M.D., Shade, P.A., Dimiduk, D.M., 2009. Plasticity of micrometer-scale single crystals in compression. Annual Review of Materials Research 39, 361–386.
Van der Giessen, E., Needleman, A., 1995. Discrete dislocation plasticity: a simple planar model. Modelling and Simulation in Materials Science and Engineering 3 (5), 689–735.
Xiang, Y., Vlassak, J.J., 2006. Bauschinger and size effects in thin-film plasticity. Acta Materialia 54 (20), 5449–5460.
Yefimov, S., Groma, I., Van der Giessen, E., 2004. A comparison of a statistical-mechanics based plasticity model with discrete dislocation plasticity calculations. Journal of the Mechanics and Physics of Solids 52 (2), 279–300.
Zaiser, M., Miguel, M.C., Groma, I., 2001. Statistical dynamics of dislocation systems: the influence of dislocation-dislocation correlations. Physical Review B – Condensed Matter and Materials Physics 64 (22), 2241021–2241029.